Modern Physics Letters B
Vol. 29, No. 33 (2015) 1550218 (10 pages)

DOI: 10.1142/S0217984915502188

Tuning the Fano resonances in a single defect nanocavity coupled with a plasmonic waveguide for sensing applications

Tiesheng Wu*, Yumin Liu*,†,‡, Zhongyuan Yu*, Han Ye*, Changgan Shu*, Yiwei Peng*, Jie Wang* and Huifang He*

*State Key Laboratory of Information Photonics and Optical Communications, Beijing University of Posts and Telecommunications, Beijing 100876, China
†State Key Laboratory of Integrated Optoelectronics, Institute of Semiconductors, Chinese Academy of Sciences, Beijing 100083, China
‡microliuyumin@hotmail.com

Received 17 January 2015
Revised 27 April 2015
Accepted 5 June 2015
Published 10 December 2015

A novel surface plasmon polaritons (SPPs) refractive index sensor based on a single defect nanocavity coupled with a metal–insulator–metal (MIM) waveguide is proposed and numerically simulated by using the finite difference time domain (FDTD) method with perfectly matched layer absorbing boundary condition. It is found that the defect structure can realize two Fano resonances and these two Fano resonances originate from two different mechanisms. The results demonstrate the liner correlation between the resonance wavelengths of the device and the refractive index of the material under sensing. Through the optimization of structural parameters, we achieve a theoretical value of the refractive index sensitivity as high as 1800.4 nmRIU^{-1}. It could be utilized to develop ultra-compact nanodevice for high-resolution biological sensing.

Keywords: Surface plasmons; optical sensing and sensors; optical resonators; integrated optics devices.

1. Introduction

By using optical components and optical principle, optical sensor can detect various physical parameters, such as displacement, weight, temperature, etc. At present, surface plasmon polaritons (SPPs) can be used in the field of nanometer sensing. SPPs are electromagnetic waves coupled to propagate free electron oscillations at metal–dielectric or metal–air interfaces. SPPs are shorter in wavelength than the incident light (photons). Hence, SPPs can have tighter spatial confinement and

‡Corresponding author.

higher local field intensity.[1−3] Because it can overcome the limit of traditional optical diffraction and manipulate optical wave on sub-wavelength,[4] these prominent features make for integration of SPPs sensor. SPPs sensors have been widely studied over the last few decades for biological and chemical sensing applications. Both SPPs and localized surface plasmon resonances (LSPR) exhibit very interesting properties for sensing applications due to their high degree of tenability and their susceptibility to the dielectric properties of the surrounding environment.[5] In the aspect of refractive index sensing, some researchers have focused on asymmetric line shape tuning for decreasing the full width at half maximum (FWHM),[5−9] and others have concerned about improving the refractive index sensitivity,[10−14] all the research purposes are to reach lower detection limits of a sensor. Fano resonance in metallic nanostructures is a coupling effect which results from the interaction of a narrow dark resonant mode with a broad bright one, and it exhibits sharp and asymmetric spectral line shapes together with strong field enhancements,[15] and so Fano resonance significantly reduces the FWHM of the plasmon modes. In the past decade, tremendous attention was attracted to design various metallic structures to obtain Fano resonance. For example, particle lattices, oligomers, nanowire lattices and split-ring-type structures[16−22] are proposed to realize Fano resonance. But these reported structures are a little bulky, the unfavorable factor making them are not easy to integrate with chips.

In this paper, a novel SPPs refractive index sensor is proposed, which consists of a plasmonic waveguide and a single defect nanocavity, and two Fano resonances are demonstrated in this structure. Compared with array structures,[16−22] this structure is more compact and simpler. This miniaturization together with planar waveguide configurations make it easy to integrate into chips.[15] The two-dimensional (2D) finite difference time domain (FDTD) method with perfectly matched layers boundary conditions is employed to simulate and research its sensing characteristics. The relationships between the Fano resonance wavelengths and the refractive index of the material under sensing (detected sample) are analyzed. Additionally, the structural parameters impacts on sensing sensitivity are analyzed to optimize the performance of the device.

2. The Structure and Theoretical Analysis

A schematic view of the proposed 2D SPPs refractive index sensor is shown in Fig. 1, which consists of a plasmonic waveguide and a rectangular cavity with a single defect on one edge. The yellow, gray and white parts in Fig. 1 represent silver, silica and air, respectively. The width of the metal–insulator–metal (MIM) waveguide is d. The length and height of the nanocavity are L and H, respectively. The width and height of the defect are w ($w \ll L$) and h, respectively. One way to fabricate this structure is by the focused ion beam (Strata FIB201, FEI Company) on a 100 nm thick silver film that is sputtered on a quartz substrate, and the other way is by depositing 100 nm silver and then etching silver film, which are described

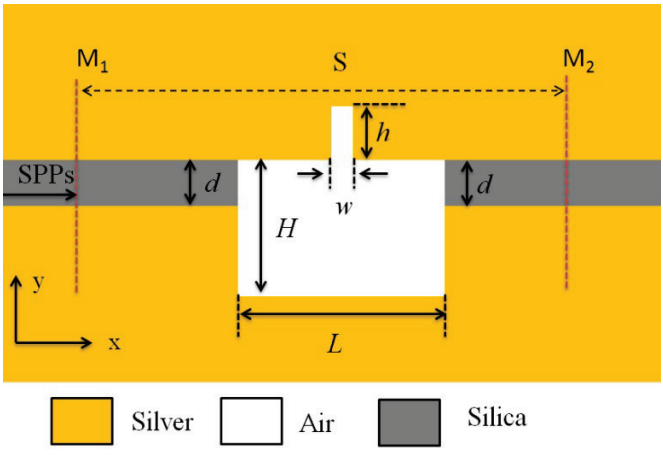

Fig. 1. (Color online) Schematic of the single defect rectangular cavity side-coupled with a MIM waveguide.

in detail in Refs. 23–25. The light can be coupled into the sensor by nano-fiber and the output light can be detected by JY Confocal Raman Microscopy.[10] As is well known, the dispersion relation of the fundamental TM mode in the MIM waveguide is determined by the following equations[4,10–12,26]

$$\varepsilon_{\text{in}} k_{z2} + \varepsilon_m k_{z1} \coth\left(-\frac{ik_{z1}}{2} d\right) = 0\,, \tag{1}$$

with K_{z1} and K_{z2} are defined by momentum conservations

$$K_{z1}^2 = \varepsilon_{\text{in}} K_0^2 - \beta^2\,, \tag{2}$$

$$K_{z2}^2 = \varepsilon_m K_0^2 - \beta^2\,, \tag{3}$$

where $\varepsilon_{\text{in}} (\varepsilon_{\text{in}} = n^2)$ and ε_m are, respectively, dielectric constants of the insulator and the metal. β is the propagation constant of the waveguide for SPPs and $k_0 = 2\pi/\lambda$ is the free-space wave vector.

In the rectangle cavity, the accumulated phase-shift per round trip for the SPPs can be given as[15,26,27]

$$\Phi = \frac{4\pi n_{\text{eff}} \times L}{\lambda + 2\varphi}\,. \tag{4}$$

Constructive interference should occur when Φ equals $2m\pi$, and thus the resonant wavelength can be described as

$$\lambda = \frac{2n_{\text{eff}} L}{(m - \varphi/\pi)}\,, \tag{5}$$

where n_{eff} is the effective refractive index of the SPPs, φ is the phase shift of the SPPs reflected off the metal wall at the end of the nanocavity and m is an integer

representing the resonant order. According to Eq. (5), the resonant wavelength will shift when the effective refractive index of the SPPs changes.

In order to investigate the sensing characteristics of the structure, its transmission spectra are simulated by using the 2D FDTD method with perfect matched layer boundary conditions. In the simulations, the structural parameters d and w are fixed to be $d = 50$ nm and $w = 20$ nm, respectively. The grid sizes in x and y-directions are set to be $\Delta x = \Delta y = 5$ nm. The fundamental TM mode of the SPPs is excited by a mode source on the left port. Two power monitors are, respectively, set at the points of M_1 and M_2 to detect the incident power P_{in} (without the resonant cavity for reference) and the transmission power P_{out} (with the resonant cavity). The distance between M_1 and M_2 is set to be 1400 nm. The transmittance of the sensor is defined to be $T = P_{\text{out}}/P_{\text{in}}$. The complex refractive index of silver and silica as functions of λ are taken from the experiment results (Palik) and expanded by using the method of interpolation.[28]

3. Simulation Results and Discussions

First, we set the structural parameters to be $L = 620$ nm, $H = 275$ nm and $h = 60$ nm, and then calculate the transmission spectra of the nanocavity with a single defect and the transmission spectra of the nanocavity (without defect), respectively. The calculated transmission spectra are displayed in Figs. 2(a) and 2(b). Obviously, two Fano resonances together with a broad Lorentzian resonant mode are observed in the transmission spectra of the defect nanocavity. But, only one Fano resonance

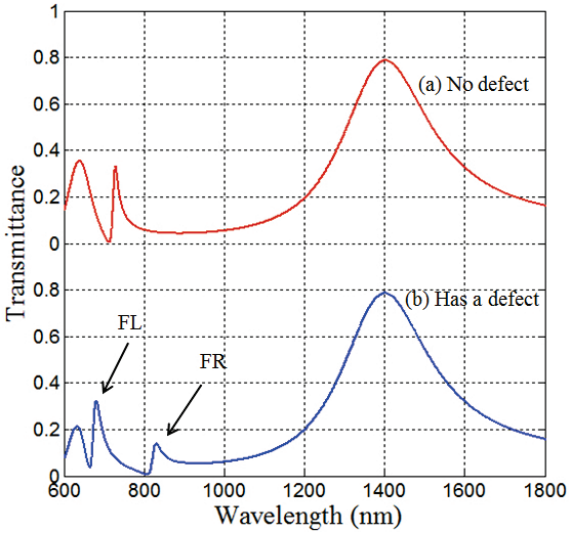

Fig. 2. (Color online) Transmission spectra of the nanocavity coupled with a plasmonic waveguide (a) without defect, (b) with a single defect. The structural parameters are set to be $L = 620$ nm, $H = 275$ nm and $h = 60$ nm, respectively.

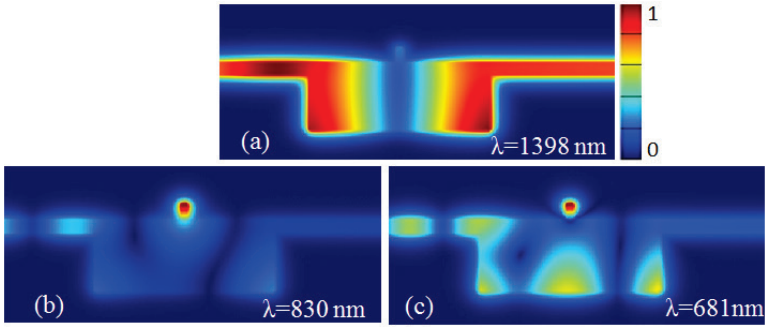

Fig. 3. (Color online) The contour profiles of field H_z of the nanocavity with a single defect at the resonant wavelengths of (a) $\lambda = 1398$ nm, (b) $\lambda = 830$ nm and (c) $\lambda = 68$ nm. The structural parameters are set to be $L = 620$ nm, $H = 275$ nm and $h = 60$ nm, respectively.

is observed in the transmission spectra of the without-defect nanocavity. We can see that the Lorantzian resonant mode exhibits a broadband transmission spectrum with a nearly symmetric Lorentzian-like profile, as shown in Fig. 2. Additionally, the field $|H_z|$ distribution in the defect rectangular cavity at the resonant wavelength for the mode is displayed in Fig. 3(a), revealing a two-order resonant mode (two antinodes in the standing wave pattern) in the nanocavity. Thus, the Lorentzian resonant mode is supported in the rectangular cavity. The field $|H_z|$ distribution in the defect rectangular cavity at the resonant wavelength for the left Fano resonance (denoted by FL, $\lambda = 681$ nm) is displayed in Fig. 3(c). Obviously, a standing wave pattern with strong intensities is excited in the nanocavity because of the structural breaking. There are three antinodes in the standing wave pattern, revealing that a high-order resonant mode (three-order oscillation) is excited in the nanocavity. The high-order resonant mode is a strong trapped mode with a narrow-band response spectrum. In the nanocavity, the narrow high-order resonant mode will interfere with the broad low-order mode, resulting in the left Fano resonance. The field $|H_z|$ distribution at the resonant wavelength for the right Fano resonance (denoted by FR, $\lambda = 830$ nm) is displayed in Fig. 3(b). It is evident that a strong field distribution is observed in the small defect (one antinode in the standing wave pattern). This reveals that the small defect supports a resonant mode (one-order oscillation) with a narrowband response spectrum.[29] This resonant mode is an inherent mode in the small stub defect and its resonant wavelength is determined by the stub dimension.[30] This narrow inherent mode in the small stub defect couples with the broad Lorentzian mode in the rectangular nanocavity, resulting in the right Fano resonance.[15]

Figures 4(a)–4(d) show the transmission spectra of the SPPs sensor by varying rectangular cavity lengths of L. The structural parameters are set to be $H = 275$ nm and $h = 60$ nm, respectively. As can be seen from Figs. 4(a)–4(d), two Fano resonances together with a Lorentzian resonant mode are observed in each of the transmission spectra. The broad Lorentzian resonant mode and the left Fano

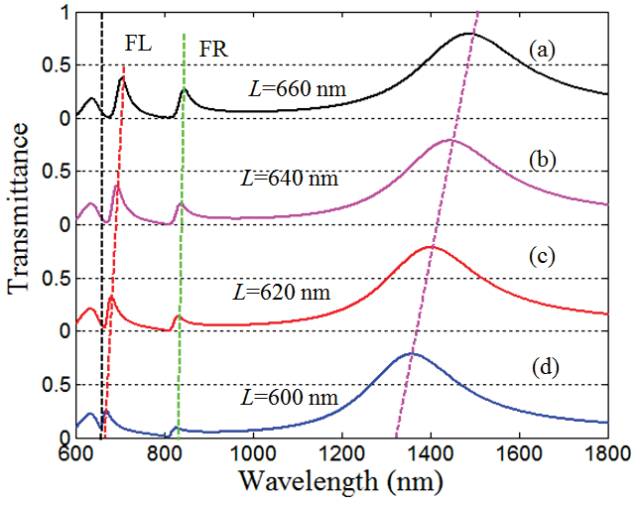

Fig. 4. (Color online) Transmission spectra of the SPPs sensor for different cavity lengths of (a) $L = 660$ nm, (b) $L = 640$ nm, (c) $L = 620$ nm and (d) $L = 600$ nm when the structural parameters are set to be $H = 275$ nm and $h = 60$ nm.

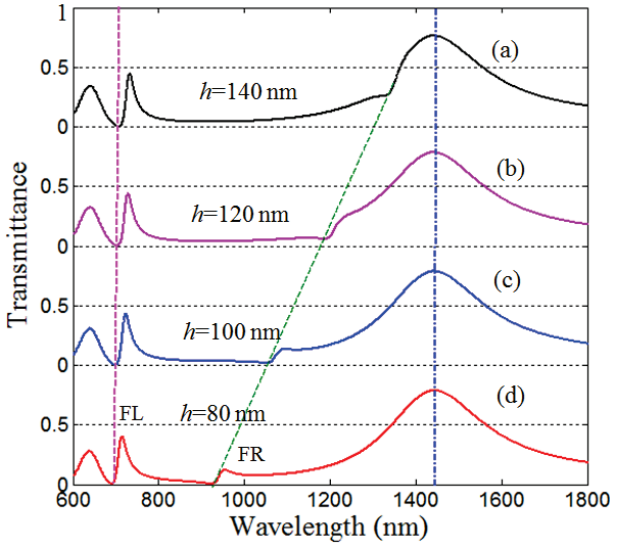

Fig. 5. (Color online) Transmission spectra of the SPPs sensor for different defect heights of (a) $h = 140$ nm, (b) $h = 120$ nm, (c) $h = 100$ nm and (d) $h = 80$ nm when the structural parameters are set to be $L = 640$ nm and $H = 275$ nm.

resonance are linearly redshift with increasing cavity length. However, the position change of the right Fano resonance is not obvious. Figures 5(a)–5(d) show the transmission spectra of the SPPs sensor with different defect heights of h. The length and height of the nanocavity are set to be $L = 640$ nm and $H = 275$ nm,

respectively. It is found that the broad Lorentzian resonant mode in the rectangular cavity is hardly varied because its resonant wavelength is determined by the fixed values of L and H. However, the situation becomes quite different for the right Fano resonance, it gives rise to greatly redshift with increasing the defect height of h. Increasing h can greatly redshift the resonant wavelength of the inherent resonant mode in the defect. Hence, the right Fano resonance, resulting from the coupling between the inherent resonant mode in the small defect and the broad low-order resonant mode in the nanocavity, is linearly redshifted when the height of the defect increases.[15]

Because the FWHM of the broad Lorentzian resonant mode is too big ($\Delta\lambda_{\mathrm{FWHM}} \approx 284$ nm), this is disadvantageous for the sensing applications. Therefore, we only intend to study the sensing characteristics of the left Fano resonance and the right Fano resonance in this structure. We fix the structural parameters to be $L = 640$ nm, $H = 275$ nm and $h = 60$ nm, and the refraction index of the detected sample is set to be $n = 1.1$. The effect of the detected sample filled area on the sensing sensitivity is shown in Fig. 6. When the detected sample is only filled in the defect, the shifts of the left Fano resonance wavelength and the right Fano resonance wavelength are 12.236 nm and 30.419 nm, respectively. When the detected sample is only filled in the rectangular cavity, the shifts of the left Fano resonance wavelength and the right Fano resonance wavelength are 49.948 nm and 57.594 nm, respectively. When the rectangular cavity and the defect are filled with the detected sample, the shifts of the left Fano resonance wavelength and the right Fano resonance wavelength are 65.405 nm and 81.217 nm, respectively. Obviously, the sensor is more sensitive when both of the rectangular cavity and the defect are filled with the detected sample. In the following analysis, assuming that both of the rectangular cavity and the defect are filled with the detected sample. Figure 7(a)

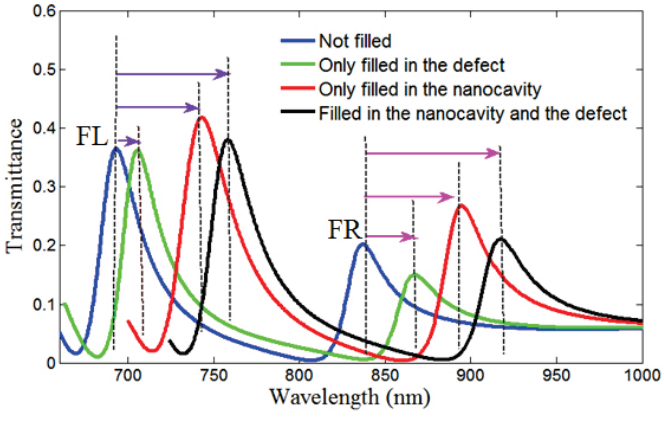

Fig. 6. (Color online) Transmission spectra of the SPPs sensor for the FL and the FR with different filled area when $L = 640$ nm, $H = 275$ nm, $h = 60$ nm and the refraction index of the detected sampled is set to be $n = 1.1$.

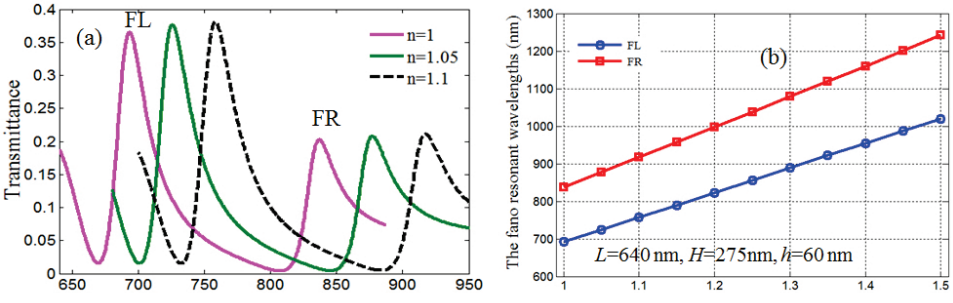

Fig. 7. (Color online) (a) Transmission spectra of the SPPs sensor for different refractive indices of the detected sample. (b) The wavelengths of the FL and the FR versus the refractive index n of the detected sample. The structural parameters are fixed to be $L = 640$ nm, $H = 275$ nm and $h = 60$ nm.

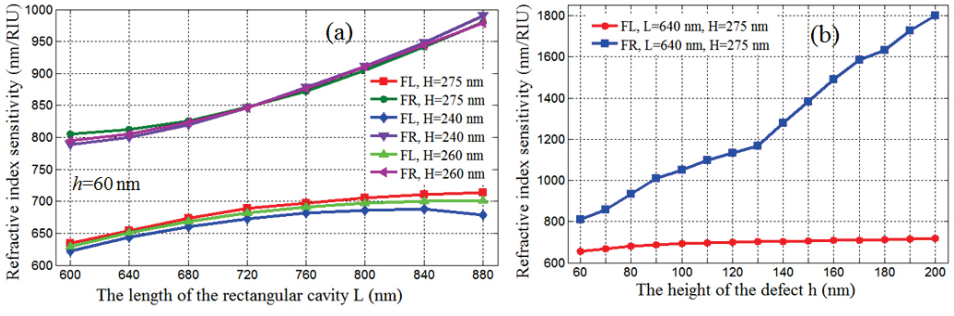

Fig. 8. (Color online) (a) The refractive index sensitivity versus the rectangular cavity length L. (b) The refractive index sensitivity versus the defect height h.

shows the transmission spectra of the SPPs sensor for different refractive indices of the detected sample from 1 to 1.1 with step of 0.05. The left Fano resonance and the right Fano resonance are redshifted with increasing the refractive index of the detected sample. Figure 7(b) reveals that the left Fano resonance wavelength and the right Fano resonance wavelength have linear relationships with the refractive index of the detected sample. The refractive index sensitivity is defined as $d\lambda/dn$, resulting in 654 nmRIU^{-1} and 812 nmRIU^{-1} for the left Fano resonance and the right Fano, respectively.

Finally, the structural parameters impacts on the sensing sensitivity are analyzed in order to improve the performance. The effects of the length of the rectangular cavity and the height of the defect on sensing sensitivity of the SPPs sensor are analyzed in detail and the calculated results are displayed in Figs. 8(a) and 8(b), respectively. It is observed that the refractive index sensitivity of the right Fano resonance increases with increasing rectangular cavity length and defect height. However, the situation becomes quite different for the left Fano resonance. It tends to be saturated when $h > 100$ nm as shown in Fig. 8(b). When structural

parameters are set to be $L = 640$ nm, $H = 275$ nm and $h = 200$ nm, the right Fano resonance would have a corresponding wavelength shift with a high sensitivity of about 1800.4 nmRIU^{-1} (700 nmRIU^{-1} in Ref. 15).

4. Conclusion

In summary, a simple SPPs refractive index sensor based on a single defect nanocavity coupled with a plasmonic waveguide is proposed. The transmission characteristics and the sensing characteristics of the single defect nanocavity are analyzed by 2D FDTD method. Simulations found that two Fano resonances are observed in the transmission spectra of the device. We would tune the two Fano resonances for sensing applications by filling the detected sample in the rectangular cavity and the defect. The results show that the Fano resonance wavelengths have linear relationships with the refractive index of the detected sample. It is especially notable that the right Fano resonance would have a corresponding wavelength shift with a high sensitivity of about 1800.4 nmRIU^{-1}. The results above imply that it have potential applications in nanoscale optical sensing.

Acknowledgments

The work was supported by the National Natural Science Foundation of China (Grant Nos. 61275201 and 61372037), Beijing Excellent Ph.D. Thesis Guidance Foundation (Grant No. 20131001301), the Fund of State Key Laboratory of Information Photonics and Optical Communications (Beijing University of Posts and Telecommunications), and the Opened Fund of the State Key Laboratory on Integrated Optoelectronics, Institute of Semiconductors, Chinese Academy of Sciences.

References

1. A. Dolatabady, N. Granpayeh and V. F. Nezhad, *Opt. Commun.* **300** (2013) 265–268.
2. C. K. Hua, Y. M. Mao and Y. Y. Yi, *Optik* **124** (2013) 4505–4508.
3. Z. D. Zhang, H. Y. Wang, Y. N. Zhao, D. Lu and Z. Y. Zhang, *Optik* **124** (2013) 177–179.
4. T. B. Wang, X. W. Wen, C. P. Yin and H. Z. Wang, *Opt. Express* **17**(26) (2009) 24096-24101.
5. K. Lodewijks, J. Ryken, W. V. Roy, G. Borghs, L. Lagae and P. V. Dorpe, *Plasmonics* **8** (2013) 1379–1385.
6. F. Hao, P. Nordlander, Y. Sonnefraud, P. V. Dorpe and S. A. Maier, *ACS Nano* **3**(3) (2009) 643–652.
7. Y. Shen, J. H. Zhou, T. R. Liu, Y. T. Tao, R. B. Jiang, M. X. Liu and G. H. Xiao, *Nat. Commun.* **4** (2013) 2381.
8. B. Gallinet and O. J. F. Martin, *ACS Nano* **7**(8) (2013) 6978–6987.
9. J. Q. Wang, C. Z. Fan, J. N. He, P. Ding, E. J. Liang and Q. Z. Xue, *Opt. Express* **21**(2) (2013) 2237–2244.
10. T. S. Wu, Y. M. Liu, Z. Y. Yu, Y. W. Peng, C. G. Shu and H. Ye, *Opt. Express* **22**(7) (2014) 7669–7677.

11. T. S. Wu, Y. M. Liu, Z. Y. Yu, Y. W. Peng, C. G. Shu and H. F. He, *Opt. Commun.* **323** (2014) 44–48.
12. J. H. Zhu, X. G. Huang, J. Tao, X. P. Jin and X. Mei, *Opt. Commun.* **285** (2012) 3242–3245.
13. V. E. Bochenkov, M. Frederiksen and D. S. Sutherland, *Opt. Express* **21**(12) (2013) 14763–14770.
14. F. Bahrami, M. Maisonneuve, M. Meunier, J. S. Aitchison and M. Mojahedi, *Opt. Express* **21**(18) (2013) 20864–20872.
15. J. J. Chen, C. W. Sun and Q. H. Gong, *Opt. Lett.* **39**(1) (2014) 52–55.
16. V. A. Fedotov, M. Rose, S. L. Prosvirnin, N. Papasimakis and N. I. Zheludev, *Phys. Rev. Lett.* **99** (2007) 147401.
17. A. Christ, O. J. F. Martin, Y. Ekinci, N. A. Gippius and S. G. Tikhodeev, *Nano Lett.* **8** (2008) 2171–2175.
18. A. Christ, Y. Ekinci, H. H. Solak, N. A. Gippius, S. G. Tikhodeev and O. J. F. Martin, *Phys. Rev. B* **76** (2007) 201405.
19. Z. K. Zhou, X. N. Peng, Z. J. Yang, Z. S. Zhang, M. Li, X. R. Su, Q. Zhang, X. Y. Shan, Q. Q. Wang and Z. Y. Zhang, *Nano Lett.* **11** (2011) 49–55.
20. J. Zhang, W. L. Bai, L. K. Cai, Y. Xu, G. F. Song and Q. Q. Gan, *Appl. Phys. Lett.* **99** (2011) 181120.
21. M. Hentschel, D. Dregely, R. Vogelgesang, H. Giessen and N. Liu, *ACS Nano* **5**(3) (2011) 2042–2050.
22. K. Aydin, I. M. Pryce and H. A. Atwater, *Opt. Express* **18** (2010) 13407–13417.
23. Q. Q. Cheng, T. Li, L. Li, S. M. Wang and S. N. Zhu, *Opt. Lett.* **39**(13) (2014) 3900–3902.
24. F. Beijnum, P. J. Veldhoven, E. J. Geluk, M. J. A. Dood, G. W. Hooft and M. P. Exter, *Phys. Rev. Lett.* **110** (2013) 206802.
25. W. W. Zhang, C. L. Zhao, J. Y. Wang and J. S. Zhang, *Opt. Express* **17**(22) (2009) 19757–19762.
26. B. Yun, G. H. Hu and Y. P. Cui, *Opt. Commun.* **284** (2011) 485–489.
27. P. X. Chen, R. S. Liang, Q. D. Huang and Y. Xu, *Opt. Commun.* **284** (2011) 4795–4799.
28. E. D. Palik (ed.), *Handbook of Optical Constants of Solids* (Academic, Orlando, FL, 1985).
29. A. E. Miroshnichenk, S. Flach and Y. S. Kivshar, *Rev. Mod. Phys.* **82** (2010) 2257–2297.
30. J. Chen, Z. Li, J. Li and Q. Gong, *Opt. Express* **19**(10) (2011) 9976–9985.